A SODIUM NITRATE - SUCROSE SOLID PROPELLANT ROCKET MOTOR DEVELOPMENT AND TESTS

Marcelo C. Tosin[1,2], F. Granziera Jr[1,2], Marília F. Chiozo[2,3], Fernando Gibim[1,2], D. L.Gazzoni Filho[1,2], A. Deliberador[2], E. Rigon[2]

[1] Electrical Engineering Dept - CTU,
[2] Nucleus of Aerospace Activities – CTU,
[3] Computer Science Dept – CCE,
Londrina State University

Rod. Celso Garcia Cid, km 380,
Londrina – Paraná – Brazil, CEP 86051 - 990
E-mail: mctosin@uel.br

ABSTRACT

This article presents the development and testing of a Sodium Nitrate - Sucrose solid propellant rocket engine. The engine is part of a main project whose goal is the construction of a small sounding rocket, capable of launching a 2 kg payload with an initial mass of 15 kg above 4000 m. This article also presents the engine project design and theoretical calculations to meet the requirements cited above. It also discusses the propellant's manufacturing process details and how they relate to the engine's performance. Safety of handling and easy manufacturing procedure were key to our choice of propellant. Tests were carried out in a small test rig to measure the engine's thrust, external temperature and two-dimensional transversal vibration. We present these performance figures and compare them to the expected theoretical results including total impulse, vibration and the thrust chamber's heat shield effectiveness. Results indicate the engine and its propellant are suitable to this kind of application and they have met the project's requirements.

INTRODUCTION

The Vetor Project is aimed at building a sounding rocket capable of launching and recovering didactical-scientific experiences with a maximum payload of 2 kg, to a height near 4000 m, with a maximum starting mass of 15 kg. Given this goal, we designed, built and tested a prototype reusable rocket motor, propelled by a sodium nitrate-sucrose composite grain. We called this prototype M44.

The propellant's choice was driven by its excellent safety properties throughout all manufacturing and usage stages, while employing standard gear for its manufacturing and handling, given that its components are non-toxic and the manufacturing process is straightforward.

Static test results on this motor attained a specific impulse (I_s) value of ~101 s. This value is significantly higher than the one found in literature – similar tests reported I_s ~71 s under the same propellant combustion conditions[1]. M44 bench tests also pointed to a significant improvement on the reproducibility and stability of the thrust curves measured. Evidence will be presented to link this performance enhancement to optimization and improved control of the propellant grain's manufacturing parameters, resizing of the convergent-divergent nozzle and thermal isolation of the combustion chamber.

Although this propellant's specific impulse is relatively low if compared to other commonly employed composites, results show that said propellant is capable of meeting all design goals, rendering it an excellent choice for this application.

MOTOR SIZING

A motor should generate enough impulse during its operating time so as to meet operational requirements for the rocket to be propelled. In order to assess the amount of propellant mass needed for this task, one must know the specific impulse produced by the propellant under motor burn conditions. This can be seen through equations (1) and (2) below.

$$I_t = \int \tau \, dt \tag{1}$$

$$I_s = \frac{I_t}{m_p g} \tag{2}$$

where, I_t, τ, I_s, m_p and g are the total and specific impulse, the motor's thrust, the mass of propellant and the gravity constant, respectively.

Specific impulse depends directly on the propellant employed, as well as burn conditions in the combustion chamber. The higher the specific impulse, the less propellant mass must be loaded onboard the rocket to fulfill its task.

Upon dimensioning the motor, we will estimate its performance and theoretical specific impulse for the propellant under standard motor operation conditions.

The propellant employed is a sodium nitrate-sucrose 3:2 mass ratio composite. Table I shows the thermodynamic parameters of the propellant's byproducts when burned at a given pressure[2]. These parameters are:

- P_o: Propellant's burn pressure
- T_o: Stagnation temperature
- γ: Specific heat ratio
- χ: Fraction of gaseous mass generated during combustion
- $\overline{M}$: Average molecular mass of combustion byproducts

Table I. Thermodynamic parameters as functions of pressure of combustion byproducts of a solid mixture of sodium nitrate and sucrose in a 3:2 ratio.

P_0 (Mpa)	T_0 (K)	γ	χ	$\overline{M}$ (kg/mol)
0.506625	1550	1.1791	0.8402	0.02783
1.013250	1615	1.1712	0.8145	0.02762
2.026500	1677	1.1639	0.7894	0.02742
4.053000	1732	1.1578	0.7672	0.02730
10.132500	1785	1.1519	0.7434	0.02697
15.198750	1802	1.1501	0.7362	0.02690
20.265000	1811	1.1491	0.7321	0.02685

Analysis of post-burn gaseous mass coefficient figures indicate an exponential decay with pressure, meaning that as

burn pressure increases, more solid byproducts are generated. Thus a relatively low burn pressure is desired, since solid byproducts contribute very little to thrust generation. With this in mind and the possibility of performance data comparison with a similar motor[1], we settled on an operating pressure of P_o = 2.0265 MPa (20 atm).

The propellant is molded as a hollow cylinder which burns in an unrestricted manner inside the motor. This produces a regressive thrust, since burn area A_b decreases with time, leading P_o to decrease as well. Thus the linear propellant burn rate R_s decreases, which in turn increases propellant burn times. This is shown by equations (9) and (3), respectively[3,4,5]. However, to facilitate motor modeling, a constant pressure P_o was employed. This implies an upper bound for total and specific theoretical motor impulse.

The linear burn rate R_s depends on pressure alone and can be modeled by equation (3) below.

$$R_s = ea \left(\frac{P_o}{P_a} \right)^n \qquad (3)$$

where e, a and n are experimentally determined constants[2] and P_a is the Pascal to atmospheres conversion factor. Table II presents figures for constants and initial parameters employed during modeling, and the theoretical computed parameters for the motor.

Table II. Figures for constants and initial parameters employed during motor modeling, and computed design parameters.

Parameter	Value	Description
M_t	15 kg	Maximum total rocket mass
D_f	0.1 m	Rocket diameter
D_{in}	0.01 m	Hollow cylinder grain's inner diameter
D_{ex}	0.079 m	Hollow cylinder grain's outer diameter
h	0.54 m	Propellant grain height
m_p	4.5 kg	Initial propellant mass
P_a	1.01325×10^5 Pa	Sea level atmospheric pressure
P_o	20.265×10^5 Pa	In-burn starting combustion pressure
e	1.4	In-burn propellant's erosion coefficient
a	7.3×10^{-4} m/s	Burn coefficient
n	0.51	Burn exponent
R_s	4.71×10^{-3} m/s	Linear propellant burn rate
ρ_p	1730 kg/m^3	Propellant density
A_{bm}	0.151 m^2	Average propellant grain burn area

T_q	3.7 s	Estimated burn time
R	8.3143 J/mol K	Universal gas constant
A_t	5.3273×10^{-4} m^2	Motor throat area
D_t	2.6×10^{-2} m	Motor throat diameter
A_e	2×10^{-3} m^2	Nozzle exit area
D_e	5.08×10^{-2} m	Nozzle exit diameter
D_c	0.100 m	Combustion chamber's external diameter
δ	0.002 m	Combustion chamber's wall thickness
h_c	0.550 m	Combustion chamber length
α	16.3°	Nozzle's divergent section angle
β	36°	Nozzle's convergent section angle
τ	1.5×10^3 N	Medium Thrust
I_t	5550 Ns	Theoretical total impulse
I_s	125.9 s	Theoretical specific impulse

The propellant cylinder's burn area A_b varies with time and can be modeled as follows:

$$A_b(t) = A_{bi} - 12\pi \ (D_{ex} + D_{in}) \ S(t) \qquad (4)$$

where:

$$A_{bi} = \pi h \ (D_{ex} + D_{in}) + \frac{\pi}{2} \left(D_{ex}^2 - D_{in}^2 \right) \qquad (5)$$

$$S(t) = \int_0^t R_s(t) \, dt \qquad (6)$$

By equations (4), (5) and (6), burn area corresponds initially to the cylinder's surface area A_{bi} minus the area reduction due to the amount of burned propellant up to time t. For D_{ex} and D_{in} the external and internal diameters of the propellant cylinder, h the propellant height and t the elapsed time. It is also true that $0 \le t \le T_q$, with T_q the total burn time.

As previously mentioned, for motor modeling, we employed a constant combustion chamber pressure P_o, not taking into account that unrestrained propellant burn produces a significant regressive burn. This happens if the second term to the right of equation (4) isn't significant, i.e. if the height h of the propellant grain is significantly higher than the propellant diameter.

Thus, we settled on a propellant height h that meets this requirement while also meeting propellant manufacturing conditions, since starting from 3 kg of sodium nitrate and 2 kg of sucrose one can reach a processed propellant final mass higher than 45 kg, resulting in a propellant height $h = 0.54$ m.

It is a good approximation to consider that area reduction due to propellant height reduction is nearly the same as the increase in burn area caused by burning of the tips. Thus one may consider the average burn area A_{bm} as the internal and external area of the cylinder, not taking into account tip area. So:

$$A_{bm} = \pi h \left(D_{ex} + D_{in} \right) \qquad (7)$$

where $A_{bm} = 0.151$ m^2.

Burn time is a parameter dependant on linear propellant burn rate and its transversal section's geometry, as long as propellant height is significantly higher than its external diameter. Since the propellant hollow cylinder's linear burn rate is R_s and the propellant burns identically on the internal and external surface of the cylinder, it's possible to consider that the propellant will have been fully burnt when the burn front of the internal surface meets the burn front of the external surface. Given that both fronts advance at the same rate, they must meet halfway between the external and internal starting radii. Thus, burn time T_q can be defined as:

$$T_q = \frac{D_{ex} - D_{in}}{4R_s} \qquad (8)$$

leading to a T_q value of ~3.7 s.

Once initial pressure is chosen, with average burn rate in hand and employing the values on Tables I and II, one may compute the motor throat area A_t by equation (9) below[3].

$$A_t = \frac{A_{bm} p_0^{(n-1)}}{p_a^n} \frac{ea\rho_p \chi}{\sqrt{\dfrac{M}{RT_0} \gamma \left(\dfrac{2}{\gamma+1} \right)^{(\gamma+1)/(\gamma-1)}}} \qquad (9)$$

where $A_t = 5.3273 \ 10^{-4}$ m^2 and so its diameter is $D_t = 2.6 \ 10^{-2}$ m.

It is now possible to compute the nozzle's divergent section escape area A_e, using equation (10) below[6].

$$A_e = A_t \frac{\left(\dfrac{2}{\gamma+1} \right)^{1/\gamma-1} \left(\dfrac{p_o}{p_e} \right)^{1/\gamma}}{\sqrt{\left(\dfrac{\gamma+1}{\gamma-1} \right) \left[1 - \left(\dfrac{p_e}{p_o} \right)^{\gamma-1/\gamma} \right]}} \qquad (10)$$

where p_e is the nozzle's divergent section exit pressure. Assuming the rocket to be operating at sea level, we have $p_e = p_a$. Replacing this in equation (10), we have $A_e = 2 \ 10^{-3}$ m^2 and a corresponding diameter $D_e = 5.08 \ 10^{-2}$ m.

Theoretical motor thrust τ is given by equation 11[3,4].

$$\tau = \left(\frac{1 + \cos\alpha}{2} \right) \left(A_t p_o \sqrt{\frac{2\gamma^2}{\gamma-1} \left(\frac{2}{\gamma+1} \right)^{\frac{\gamma+1}{\gamma-1}} \left(1 - \left(\frac{p_e}{p_o} \right)^{\frac{\gamma-1}{\gamma}} \right)} + (p_e - p_a)A_e \right) \qquad (11)$$

where α is the angle between the divergent section and the motor's symmetry axis. For $\alpha = 16.3°$, thrust will be $\tau = 1.5$ kN.

Finally theoretical total and specific impulses can be computed by equations (1) and (2), respectively. Thus $I_t = 5550$ Ns and $I_s = 125.9$ s.

COMBUSTION CHAMBER STRUCTURAL SIZING

The rocket motor was built using SAE 1020 steel, based on previously calculated sizes. Figure II depicts the motor. The combustion chamber has cylindrical shape with internal diameter $D_c = 0.096$ m and chamber length $h_c = 0.550$ m. Motor physical dimensions are laid out in Table II.

The combustion chamber wall must be thick enough to handle the motor's operating pressure. Tension efforts can be modeled as in a cylindrical vase with external radius r and thickness δ, exposed to an internal pressure p. Thus we have[7]:

$$\sigma_\theta = \frac{pr}{\delta} \qquad (12)$$

$$\sigma_\varphi = \frac{pr}{2\delta} \qquad (13)$$

where σ_θ is tangential tension and σ_φ is longitudinal tension on the cylindrical shell.

Since σ_θ is the highest tension suffered by the cylindrical shell, and given that the tube is under an internal theoretical operating pressure $p \approx 2$ MPa, the SAE 1020 steel tensile strength is 350 MPa and the rocket tube diameter is 0.1 m, one can verify that:

$$\delta \geq f \ \frac{pr}{\sigma_\theta} = 2 \ \text{mm} \qquad (14)$$

with a safety factor $f = 7$.

COMBUSTION CHAMBER THERMAL SHIELD SIZING

During propellant combustion, high temperatures are generated which, along with operating pressure, can compromise the motor's structural integrity and reduce its life span, unless an efficient way of thermally protecting the combustion chamber structure is employed. A viable solution to this problem is a thermal isolation layer inside the chamber, which also improves motor efficiency, preventing losses by thermal dissipation through the shell.

Due to the combustion chamber's cylindrical symmetry, heat conduction through the thermal insulation layers and the engine's shell can be modeled by the equation below.

$$\left[\frac{\partial^2 T}{\partial x^2} = \frac{1}{\alpha} \frac{\partial T}{\partial t} \right] \qquad (15)$$

During engine run, its internal temperature T_0 can reach 1677 K, which is the propellant burn stagnation temperature (see Table I). Equation (16) represents the analytical solution to the temperature distribution through the heat shield only during engine run[8].

$$T(x,t) = (T_e - T_0) \ \text{erf} \left[\frac{x}{2(\alpha \ t)^{1/2}} \right] + T_0 \qquad (16)$$

where $T(x,t)$ is the temperature as a function of time and as a function of distance through the insulation barrier, α is the thermal diffusibility of the heat shield material, T_e is the temperature on the external insulation surface at instant $t = 0$ and x is the point through the insulation barrier for which the temperature at a given instant t must be calculated. The point where $x = 0$ refers to the internal insulation surface, where the temperature is T_0 at any instant t. The described model defined by equation (16) represents the temperature profile through the heat shield in a nonequilibrium heat conduction regime. This equation is only valid during engine burning time T_q. Thus, $0 \leq t \leq T_q$.

Due to constructive constraints, such as the handling of the heat shield materials inside a tube of reduced dimensions, the heat shield was dimensioned with layers of craft paper and natural latex glued to the inner surface of the combustion chamber wall. This is shown in Figure I.

Equation (16) can be used to determine the temperature distribution across the heat shield layers and the shell. The temperature points T_0, T_A, T_B, and T_C, (see Figure I) are the internal surface of the latex layer, the interface between this and the craft paper layer, the interface between the latter and the

engine's internal wall and the interface between the external shell surface and the atmosphere, respectively. With knowledge of the thermal diffusibility coefficients of these materials (see Table III), the temperature distributions over time at the points T_A, T_B, e T_C can be estimated using equation (16) as a recurrence formula, numerically calculating the temperature at these points for infinitesimal time intervals Δt. So:
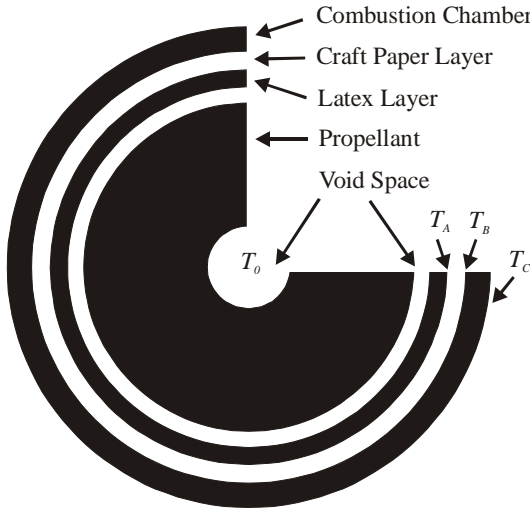
$$T_0 = 1677 \text{ K} \tag{17}$$

$$T_A(t_n) = \left[T_A(0) - T_0\right] \text{ erf}\left[\frac{\Delta x_{lat}}{2(\alpha_{lat} \ t_n)^{1/2}}\right] + T_0 \tag{18}$$

$$T_B(t_n) = \left[T_B(0) - T_A(t_n)\right] \text{ erf}\left[\frac{\Delta x_{cft}}{2(\alpha_{cft} \ t_n)^{1/2}}\right] + T_A(t_n) \tag{19}$$

$$T_C(t_n) = \left[T_C(0) - T_B(t_n)\right] \text{ erf}\left[\frac{\Delta x_{st}}{2(\alpha_{st} \ t_n)^{1/2}}\right] + T_B(t_n) \tag{20}$$

$$t_n = n \ \Delta t \quad n = 0, 1, 2, 3, ... \tag{21}$$

where Δx_{lat}, Δx_{cft} and Δx_{st} are the thickness of the latex layer, the craft paper layer and the combustion chamber wall, respectively. These figures are shown by Table III.


Figure I. Transversal section of the engine's combustion chamber, showing the configuration of the heat shield and propellant grain. Employed materials and the details of the heat shield's layers glued to the engine's internal wall are shown.

Table III. Thermal diffusibility coefficients and thicknesses of the materials employed in the combustion chamber's construction.

Parameter	Value	Description
Δx_{lat}	0.0015 m	Natural latex layer thickness
Δx_{cft}	0.0015 m	Craft paper layer thickness
Δx_{st}	0.002 m	Combustion chamber wall thickness
α_{lat}	6 10⁻⁸ m²/s	Latex thermal diffusibility coefficient
α_{cft}	1.4 10⁻⁷ m²/s	Craft paper thermal diffusibility coefficient
α_{st}	1.48 10⁻⁵ m²/s	SAE 1020 steel thermal diffusibility coefficient

Figure II shows the temperatures for points T_A, T_B and T_C as functions of time (see Figure I). These points correspond to curves (a), (b) and (c), respectively, which were generated by equations (18), (19) and (20). From curve (c) one can notice that, during the entire engine burn, the temperature on the combustion chamber structure surface remains in levels close to the environmental temperature, ensuring the physical integrity of the combustion chamber. For a burn time of ~4 s, the calculated temperature of the chamber's external surface is 298 K for a starting temperature of 292 K.
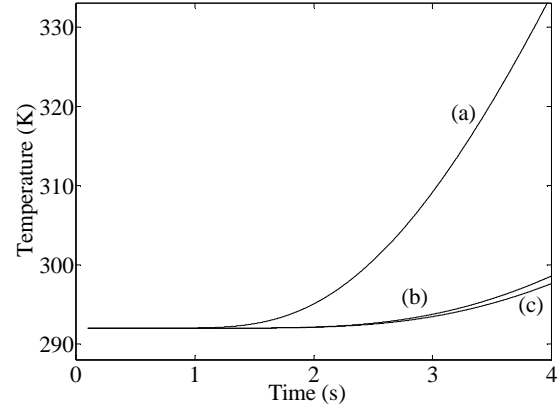
Figure II. Calculated temperature versus time curves at the interface between the internal surface of the latex layer and the craft paper layer (a), the interface between the latter and the engine's internal wall (b) and the external shell surface (c). These curves correspond to the points T_A, T_B, and T_C at Figure I, respectively.

In an earlier paper[1], bench tests performed on a similar engine revealed that its propellant's specific impulse is ~71 s, under the same burning conditions specified in the present work. This figure stands significantly below the calculated theoretical specific impulse (I_s = 125.9 s), indicating that problems with the propellant grain and with the combustion process might exist. The adoption of a heat shield not only allows for safer engine operation, but it also guarantees its physical integrity and its reusability. The shield also increases system efficiency, minimizing heat losses by the gaseous masses generated by combustion through the engine's shell.

THE PROPELLANT AND ITS MANUFACTURING PROCESS

The propellant is formed by a 3:2 mass mixture of finely grinded Sodium Nitrate and Sucrose. The powdered components are mixed until homogeneity is reached and stowed in a metallic recipient. The mixture is slowly heated and vigorously mixed until the fusion of Sucrose. This process produces a homogeneous paste that will be molded to the propellant grain's format. After solidification, the propellant grain turns into a composite formed by Sodium Nitrate particles embedded in a polycrystalline Sucrose matrix.

Ideally, the matrix must uniformly involve the oxidizing particles to produce a stable combustion and propellant burning velocity figures in accordance with values determined at the motor design phase. The obtained composite's mechanical resistance must allow it to resist mechanical and thermal stresses generated during combustion inside the motor. During the combustion, the propellant must keep a known burning area as it is consumed. All these desired characteristics are tightly

connected to the microscopic structure of the composite and how its components interact during combustion.

During the matrix solidification process, the great amount of oxidizing particles does not allow its uniform crystallization. These particles act as nucleation centers, which determines the formation and growth of the matrix polycrystalline structure[9]. This structure, depending on the system's solidification process, might favor the formation of undesirable cracks and tensions in the propellant grain. These structural failures in the grain can generate random or even abrupt variations of the burning surface, compromising the stability and reproducibility of the combustion process.

The manufacturing process of the M44 engine's propellant was developed from a process described in an earlier paper[1]. That process possessed some unsatisfactory characteristics, listed below:

• Excessive moisture absorption due to the high hygroscopic capacity of its components. The procedures performed during molding did not insulate the propellant from the atmosphere, not allowing it to be stocked.

• The molding process employed a steel frame, which cooled the propellant too quickly, potentially resulting in the formation of cracks and tensions in the structure. This increased the risk of propellant structural failures at ignition and during its combustion, possibly causing burning instabilities, such as shuffles and non-reproducibility of the thrust curve. Even the explosion of the engine could occur, due to an abrupt increase of the burn area.

• Lack of homogeneity of the mixture during its manufacturing process, resulting in agglutination of the Sodium Nitrate in the form of tiny pellets which are involved by the mixture, also causing burning irregularities.

Many procedures have been adopted in order to avoid or at least reduce the aforementioned issues. They are presented below:

• Slow cooling of the mixture. This allows for a better propellant grain crystallization, reducing the cracks and tensions in its structure, enhancing the propellant's resistance and contributing for a stabler burn. The steel frame was replaced by a craft paper mould, internally coated with acetate sheets. Once filled with the liquid propellant, the frames is sealed and stored in a refractory cylinder. This causes Sucrose to crystallize slowly.

• The mixture's temperature, formerly controlled by means of a heated oil bath, is now manually controlled and monitored by a thermometer. The heated oil bath has been replaced by a heated 10 mm thick aluminum recipient, in order to uniformly distribute the temperature. This caused a sensible simplification of the process, asides from reducing propellant contamination during the process.

• After cooling, the solid propellant is removed from the refractory cylinder, but remains encased by the mould, which prevents contact with the atmosphere. Thus, the propellant can be stocked for a period of a few days. The propellant's final mass is approximately 90 % of its components' initial mass. This is mainly due to losses during the manufacturing process.

EXPERIMENTAL PROCEDURES FOR THE ENGINE'S STATIC TESTS

In order to compare the engine's performance with the previously described theoretical models, static bench tests were performed. Thrust over time, external temperature and two-dimensional transversal vibration were measured in such tests. Figure III illustrates the experimental setup of the static tests.

The static tests were performed on a bench described elsewhere[1]. Some improvements have been made to this bench, in order to improve the electromagnetic noise immunity over the sensors installed on the engine. To this end, a grounded metallic cage was placed around the bench. The engine was mounted over the bench, generating thrust in the opposite direction to that of gravity. Thrust was measured by a load cell with a maximum capacity of 20 kN. Three K–type thermocouples have been employed in the measuring of the engine's external surface temperature at distinct points. Vibration was measured by a two-dimensional accelerometer transversally mounted on a holder glued to the combustion chamber's external surface. Figure III shows the positions of the thermocouples, the load cell and the accelerometers.
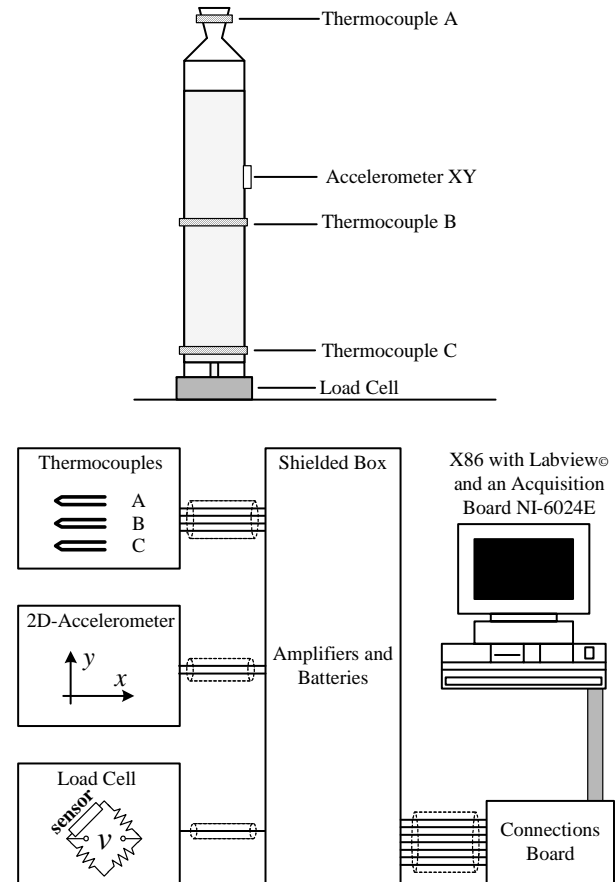
Figure III. Experimental setup of the static tests.

The output signals of the load cell and the thermocouples were amplified and conditioned using dedicated circuits installed in a grounded metallic box. The amplified output signals were input to the acquisition system's connections board. The output signals of the two-dimensional accelerometer were directly input to the connections board. Shielded cables and connectors were used to interconnect the electronic components. The thermocouples were coated with a metallic shielding over the thermo-electrical insulation of their wires. All of the system's shielding, including the engine's shell and the microcomputer with the acquisition system, was connected to the test bench's common grounding. With this careful procedure, a high noise rejection has been achieved, allowing for sensor resolution figures very close to the theoretical ideal.

The load cell's sensing element is basically a strain-gauge glued to the cell's body and with one of its ends connected to a

resistive Wheatstone bridge. For the particular cell used in the experiments, the resistance of each edge of the bridge is ~360 Ω. The working principle of a load cell is based on the variation of the strain-gauge's resistance when the cell suffers the action of a force. By applying an electrical input voltage between two opposed edges of the bridge (see Figure III), the voltage between the remaining edges must be linearly proportional to the force acting on the cell[10].

The cell used in the experiments has a sensitivity $S_1 = 1$ mV/kN, with an applied potential of 10 V. The cell's output potential must be amplified in order to achieve the highest possible resolution in the acquisition system, within a predefined load range. To this end a maximum charge of 5 kN was estimated to be applied to the cell. This is equivalent to approximately three times the calculated average engine thrust. Since the maximum output to the acquisition system is 10 V, the cell's output signal should be amplified so that its output is 10 V with an applied 5 kN load. Thus, system sensitivity after amplification should be $S_2 = 2$ V/kN. In this way, the amplifier gain applied to the signal should be :

$$G = \frac{S_2}{S_1} = 2000 \qquad (22)$$

An amplifier board was specifically assembled for this load cell and it is based on Texas Instruments' INA125 instrumentation amplifier. This amplifier also supplies the load cell with a stable reference voltage, and its gain may be adjusted using a precision variable resistor.

Several factors can cause unwanted inaccuracies in the load cell measurements, specially the temperature drift on the cell and amplifier components. So, the system should be assessed a few moments before each test. Figure IV (a) illustrates a load cell assessment procedure. In this procedure, 200 N equivalent loads were stacked and unstacked over the cell every ~5 s. Figure IV (b) shows the average voltage on the amplified load cell output during assessment.

The load cell plus amplifier transfer equation was obtained by linear regression of the points from Figure IV (b), resulting in the equation below:

$$V = 0.57 + 1.88L \qquad (23)$$

where V is the amplified voltage (V) and L is the load applied to the cell (kN).

It can be verified that the system's sensitivity is the slope of the straight line from Figure IV (b). Thus: $S_2 = 1.88$ V/kN and the applied amplifier gain (G) is ~1880.

Equation's (23) constant is related to the load cell's strain-gauge thermal drift. This effect could be explained by the constructive characteristic of the load cell which has been used. This cell employs only a single strain-gauge in the resistive bridge. Slight thermal variations on the cell can cause stress variations perceptible to the strain-gauge. Such variations unbalance the resistive Wheatstone bridge, generating a measurement offset. However, the thermal drift does not alter system sensitivity. Due to the fact engine burning time is relatively short (T_q ~4 s), that measurement offset is practically constant. It can be easily identified and subtracted from the acquired voltage values from the static tests.

The K-type thermocouples' signals were amplified and conditioned by a dedicated circuit board which was specially assembled for this task. This circuit is based on the Analog Devices' AD 595 amplifier. This amplifier compensates its output signal for cold joint and provides a sensitivity of approximately 10 mV/°C. After acquired, these output voltage signals are converted to temperature by a specific lookup table.

The engine's transversal accelerations were measured by a model ADXL202 two axis accelerometer from Analog Devices. This accelerometer was mounted on a printed circuit board and the board's reverse surface was glued to a transversally adapted holder on the combustion chamber's external surface, as indicated in Figure III. The accelerometer axes' analog outputs were directly connected to the acquisition system. This accelerometer can measure from –2 g to +2 g on both its axes, with a typical sensitivity of ~0.32 V/g.

The load cell's and the thermocouples' amplification boards were powered by a symmetrical voltage of ±12 V. The accelerometer was powered by a voltage of 5 V supplied by a regulator model TPS 76150 from Texas Instruments. The power was provided by two 12 V/2 Ah sealed lead-acid batteries and the total current drained from them was lower than 100 mA.
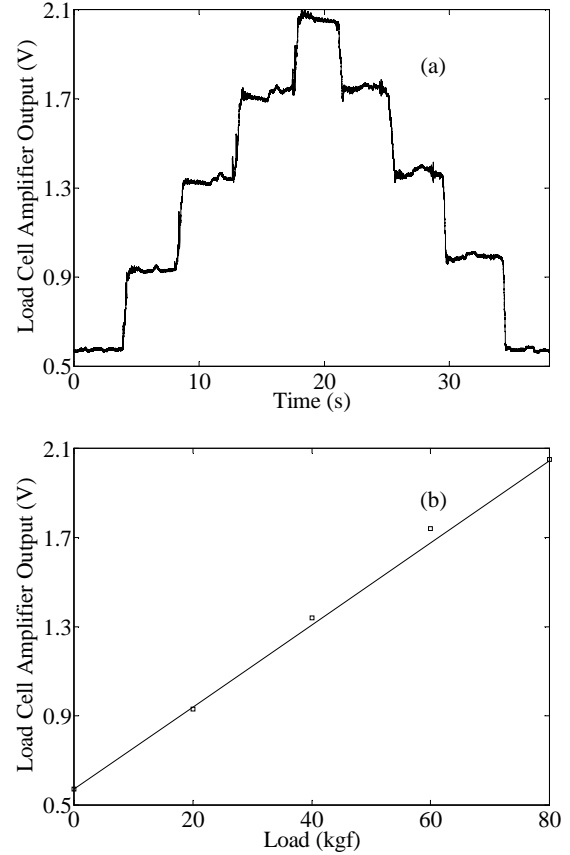
Figure IV. Load cell assessment curves. (a) Voltage at the amplifier's output due to the stacking and unstacking of 200 N weights over a ~40 s time interval. (b) Linear regression of the average voltage at the amplifier's output as a function of the applied weights.

The load cell's and thermocouples' amplified outputs and the accelerometer outputs were digitalized by an acquisition board model NI–6024E from National Instruments. This board was installed inside a x86 workstation. The acquisition system sampling rate was settled to 1000 samples per second. For controlling the static tests it was utilized the Labview 6 automation environment. A virtual instrument (V.I.) was developed to automatically acquire data and direct it to a local file. Also, this virtual instrument was capable of controlling the ignition countdown and automatically generating startup sequencing signals to the engine igniters. In order to trigger the igniters, current drivers were assembled in a separate board. These drivers were controlled by the digital outputs from the acquisition board. The power to the igniters was supplied by a

12 V/500 mA sealed lead-acid battery. The capability of being controlled via a TCP/IP over Ethernet link was also integrated to the V.I. This allowed static tests to be remotely controlled and initiated via a host computer. This control capability also improved safety.

The igniters are made of a tungsten filament assembled inside a small and thin polypropylene bag filled with 5 g of slow burning gunpowder. The gunpowder is set on fire by heating the filament by passing an electrical current through it.

M44 STATIC TESTS RESULTS AND DISCUSSION

Figure V illustrates the thrust curve (a), the calculated impulse (b) and the vibration figure (c), as functions of time. These curves were obtained during an engine's static test using a two-igniter engine setup.

Figure V (a) shows a typical thrust curve that illustrates the engine's propellant regressive burning. This decaying curve agrees with the expected behavior of an unrestricted burning surface propellant with a hollow cylinder shape[4,5]. This can be visualized through equation (4), which indicates that propellant burning area decrease with time. The latter lowers internal combustion chamber pressure (equation (9)) and, as a consequence, it also reduces the thrust generated on time (equation (10)). The maximum generated thrust is ~2 kN and it occurs slightly after the engine starts its operating regime. This curve smoothly diminishes without shuffles, indicating the propellant's burning stability during the entire working period of the engine. This is due to a careful propellant production procedure, which raised engine reliability and also raised generated thrust curve repeatability.
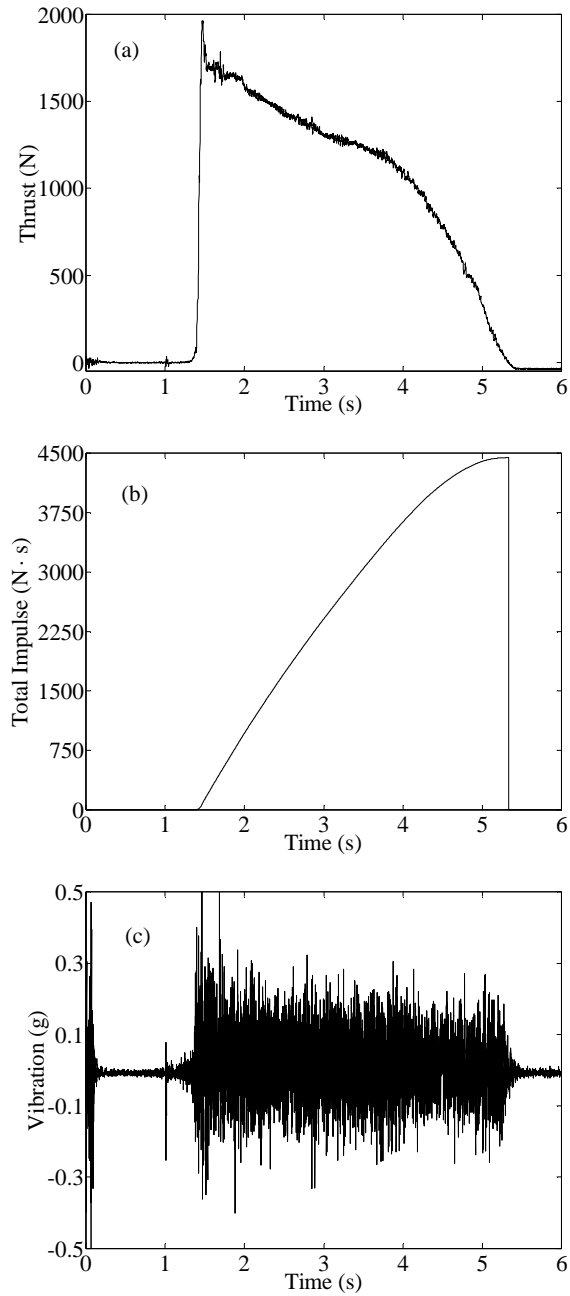
Figure V (b) shows the engine's generated impulse as function of time. This curve was calculated by the accumulated sum of the thrust curve values over time. These values refer to Figure V (a). By the end of the engine's burning time, the total generated thrust was ~4440 Ns. From this value and using equation (2), it is possible to calculate the propellant's specific impulse, thus: I_s ~101 s. These measured impulse and specific impulse values are 20 % lower than the calculated theoretical values. This could be due to the following facts:

• The engine's model described does not predict a diminishing propellant burning area during combustion. It relies on an average burning area for engine's performance values calculation. As a consequence, the model assumes a constant operating pressure during its working regime. This simplifies the engine's dimensioning calculations and the resulting values represent an upper bound to the engine's measured performance values. From equations (1), (2), (9), (10) and (11), one can visualize that if propellant's burning area decreases with time, its internal pressure diminishes. As a consequence, its generated thrust also diminishes, resulting in lower values of total impulse and specific impulse.

• The heat loss from the combustion gases to the convergent-divergent section, because only the engine's combustion chamber is thermally protected.

• The occurrence of flow separation on the divergent section surface. This is probably due to the large quantity of solid matter generated during the combustion process. Table I shows that the generated solid mass fraction varies from ~16 % to ~21 % for combustion pressures varying from ~0.5 MPa to ~2 MPa, respectively. Flow separation could be identified by visual inspection of the nozzle convergent section's surface after mechanical removal of solids adhered to it. The exit divergent section area was designed based on an overestimated value of internal pressure calculated (equation (10)). In this

way, the nozzle exhaust over-expands the exiting gases, also contributing to flow separation.

Figure V. Typical thrust curves (a), calculated impulse (b) and transversal vibration (c) as functions of time, measured during one of the engine's static tests. These curves correspond to a two-igniter engine setup.

Figure V (c) shows the engine's transversal vibration curve. For this test two igniters were utilized and fixed on the cylinder propellant extremity surfaces. Curve (c) also shows two peaks at t = 0 and t = ~1 s, corresponding to the instants where igniters were triggered. The first peak corresponds to the igniter deeper within the combustion chamber and the second one corresponds to the igniter closer to the convergent section. Approximately 350 ms after triggering the second igniter, the engine starts its operating regime. In this period it is possible to visualize the vibration caused by the beginning of propellant combustion inside the chamber. This starting vibration has an

amplitude of ~0.02 g, which grows abruptly when engine enters its operating regime. The vibration amplitude at the working regime is ~0.15 g (see Figure V (c)). A pressurization seal is not utilized inside the throat. This demonstrates the propellant grain has good ignitability. Once in operating regime, the engine's vibration extends for a period of ~4 s, corresponding to the period in which it produces thrust. This can be visualized by comparison of Figures V (a) and (c). Curve (c) keeps a uniform vibration pattern during operating regime. This is indicative of a good burning stability without shuffles, which agrees with the observed thrust curve (Figure V(a)).
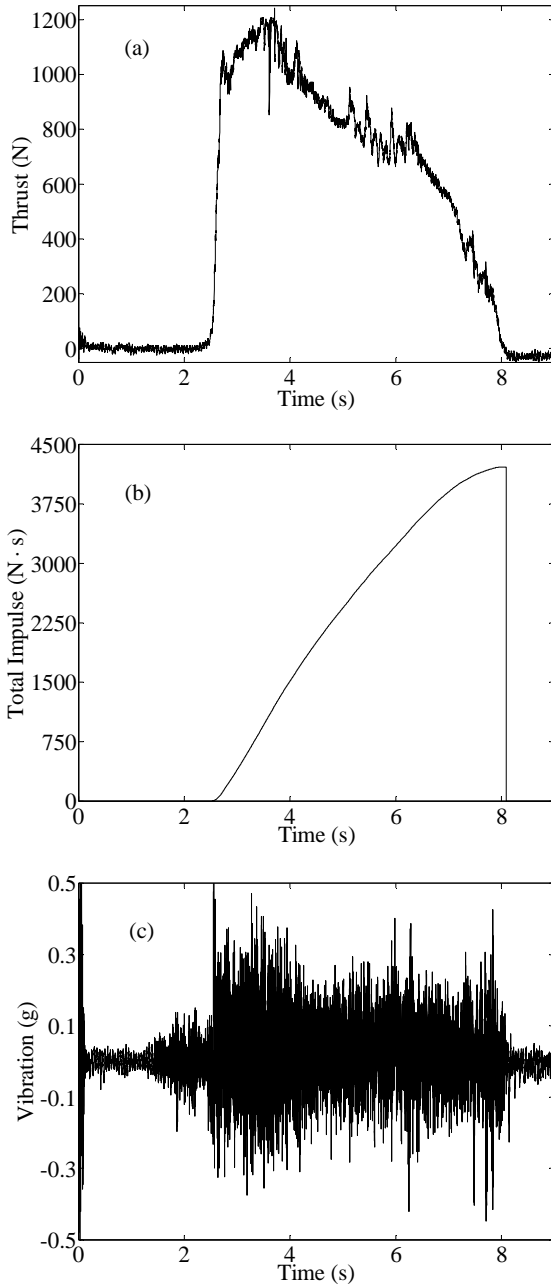

Figure VI. Typical thrust curves (a), calculated impulse (b) and transversal vibration (c) as functions of time, measured during one of the engine's static tests. These curves correspond to a single-igniter engine setup.

Figures VI illustrate the thrust curve (a), the impulse curve (b) and the vibration curve (c) for a static test where the engine

was setup with a single igniter. The igniter was fixed on one of propellant extremities' surface and placed close to the bottom of combustion chamber. After curves (a) and (b), one can notice a significant rise on the engine's burning time, which was ~5.4 s. Despite a longer burning time, Figure VI (b) shows a total impulse of ~4300 Ns. This value is 3 % smaller than the total impulse obtained for engine firing with two igniters. This shows that the way the engine is ignited has a considerable influence on the engine's propellant burning pattern, despite the total impulse being approximately the same. With a two-igniter setup, the propellant surface is initially set on fire uniformly, producing ~4 s of burning period. This burning time is very close the one calculated using the model described by equation (8), where $Tq = 3.7$ s. Figure VI (a) shows a regressive thrust curve with no shuffles. However, this curve also shows the occurrence of small instabilities when compared to Figure V (a). These instabilities are characterized by the small peaks and variations over the thrust curve. Also, this can be visualized by comparison between Figure V (c) and Figure VI (c). One might notice that the vibration pattern for the engine fired with two igniters is more uniform than the vibration pattern for a single igniter. It must be emphasized that visual comparison between these vibration patterns is preliminary and qualitative. In order to correlate these vibration patterns a greater experimental effort is needed.

In a second comparison between Figure VI (a) and Figure V (a) it is possible to visualize that both curves have the same basic shape. One can notice the thrust generated during the burning time for the engine with a single igniter has a smaller magnitude than thrust generated by the engine configured with two igniters. This fact allows this engine to be utilized on applications where smaller accelerations are needed, but generating almost the same impulse.
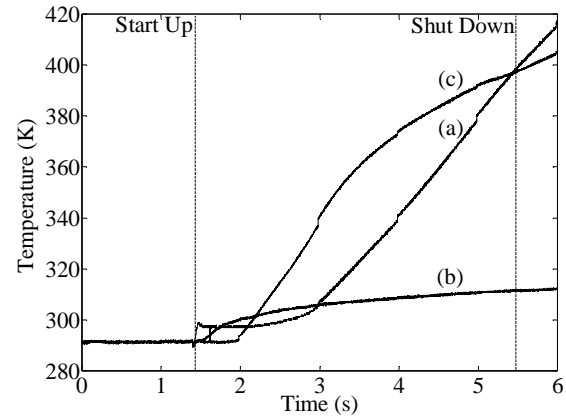
Figure VII. Temperature curves for different points of the engine's external surface, measured during engine burn time in a static test. Curves (a), (b) and (c) correspond to the points measured by thermocouples A, B and C, respectively. Thermocouple installation points can be identified from Figure III.

Figure VII shows temperature curves on the engine's external surface, measured during a static test. These measurements have been taken of the engine when using the two-igniter setup, with a burning time of approximately 4 s. The points where temperature was measured can be seen in Figure III. Figure VII (a) shows the temperature close to the end of the nozzle's divergent section. By the burn's end, this temperature is ~399 K. It continues to raise due to heat transferred from the convergent section. Curve (b) shows the external combustion chamber temperature in the middle

section. By the burn's end, this temperature is ~312 K. Finally, curve (c) shows how temperature changes in the lower portion of the combustion chamber, reaching ~398 K by the burn's end. These curves show that heat shield performance is satisfactory in that it keeps combustion chamber temperature within acceptable levels during propellant burn. This ensures the engine tube's physical integrity while the combustion chamber is pressurized and at a calculated internal temperature of ~1677 K. After the burn, the chamber's temperature still rises, due to heat transfer from the nozzle. This is because the convergent-divergent section is screwed to the combustion chamber, and only the latter is equipped with heat shielding.

One can see by comparison between Figure VII (c) and Figure VII (b), the temperatures on the surface next to the bottom of combustion chamber are grater than the temperatures on its surface at middle portion. The motor tube used has a diameter of 0.098 m and a height of 0.60 m. The bottom of the tube is sealed and it confers to the bottom of combustion chamber a spherical shape. Thus, the only way to access the combustion chamber interior is by the other extremity of the motor tube, where the nozzle is screwed. The tube dimensions and its internal shape make the confection and assembly of the thermal shield a difficult task, especially due to combustion chamber spherical bottom. For this reason the heat shield inside the combustion chamber bottom is less efficient than the shield at the wall.

Due to the facts described above, the heat conduction on the chamber surface's middle portion is the closest to the one-dimensional heat conduction model. This can be seen by comparison between Figure VII (b) and Figure II (c), where the measured temperature at engine's burn end is ~312 K. This value is close to the calculated value, which is ~298 K.

PERFORMANCE SIMULATION FOR A M44 PROPELLED ROCKET

The M44 engine was designed aiming to propel an experimental rocket to a height of approximately 4000 m from its launch base. The rocket's principal diameter is 0.1 m and it should be capable of transporting an up to 2 kg payload, with a maximum initial mass of 15 kg.

In order to determine whether the engine will be able to carry out the mission it was designed for, a vehicle flight simulation algorithm has been implemented. The simulation uses experimentally collected data from static tests.

For this simulation, the following assumptions will be made: (i) the launch angle is more than 85°; (ii) the rocket's trajectory is practically rectilinear while the engine is working; (iii) when the engine is no longer working, the trajectory described by the rocket is close to a steep parabola, consequently exhibiting a very long vertical displacement. It can be verified that the acceleration, velocity and axial displacement time-dependant parameters can be approximated by the same parameters taken at the vertical coordinate of the rocket's gravity center during flight. In this way, the system can be described by a single-dimension model where, from discrete thrust data and given initial parameters, the system's variables are calculated by an iterative process. The number of iterations is a function of simulation time and sampling rate.

These are the simulation parameters:
- m_i, the rocket's initial mass;
- I_s, the specific impulse;
- g, the acceleration of gravity;
- t_q, the burn time;

- $E[n]$, the discrete thrust (experimentally acquired data).

Total impulse I_t can be calculated as the numeric integral of the discrete thrust. Thus, the total propellant mass can be calculated using equation (2), as seen below:

$$I_t = \sum_{k=1}^{t_q/T} E[k] \qquad (24)$$

$$m_p = \frac{I_t}{gI_s} \qquad (25)$$

where T is the sampling period for the thrust data and t_q/T is the amount of samples during the engine's burn time.

Using these data and the accumulated sum of the thrust array it is possible to calculate the vehicle's mass at each instant nT and store it in a single-dimension array $m[n]$, thus:

$$m[n] = m_i - m_p \frac{T}{I_t} \sum_{k=1}^{n} E[k] \qquad (26)$$

Consequently, the weight array can be calculated, as shown below:

$$P[n] = g\, m[n] \qquad (27)$$

The resultant force can be obtained from an analysis of the forces to which the rocket is subject:

$$F_r[n] = E[n] - P[n] - F_d[n] \qquad (28)$$

where F_d, the force due to aerodynamic drag, can be defined as:

$$F_d[n] = \frac{1}{2} C_d A \rho[n] \left(v[n]\right)^2 \qquad (29)$$

where $\rho[n]$, $v[n]$, C_d and A are the discrete atmospheric density, the discrete vehicle velocity, the aerodynamic drag coefficient and the rocket's principal transversal section area, respectively.

Atmospheric density varies with altitude and temperature. So, the discrete atmospheric density can be described as[11]:

$$\rho[n] = \rho_0 \left[1 - \frac{\lambda}{T_0}\left(h_0 + h[n]\right)\right]^{\left(1 - \lambda R/\lambda R\right)} \qquad (30)$$

where:
- h_0, the launch altitude;
- ρ_0, the air density at the launch altitude;
- T_0, the air temperature at the launch altitude;
- λ, the temperature-altitude gradient;
- R, the gas constant for the air;
- $h[n]$, the discrete height reached by the rocket from the launch height h_0.

For a velocity up to ~238 m/s, the rocket's C_d can be taken as a constant. If the velocity is between ~238 m/s and ~442 m/s, the C_d varies linearly in relation to the natural logarithm of velocity[12]. So, the discrete aerodynamic drag can be defined as:

$$C_d[n] = \begin{cases} 0.23 \\ \quad \text{if } v[n] < 238 \text{ m/s} \\ \\ 0.00323 \ln\left(v[n]/340\right) + 0.3452 \\ \quad \text{if } 238 \text{ m/s} < v[n] < 442 \text{ m/s} \end{cases} \qquad (31)$$

Discrete acceleration can be calculated from Newton's laws, where:

$$acc[n] = \frac{F_r[n]}{m[n]} \tag{32}$$

Discrete velocity and height should be calculated from the numerical integration of discrete acceleration, as shown below:

$$v[n] = T \sum_{k=1}^{n} acc[k] \tag{33}$$

$$h[n] = T \sum_{k=1}^{n} v[k] \tag{34}$$

Taking initial values $v[1] = 0$ and $h[1] = 0$, the equations above can be iteratively applied to arrays of n integer values, where $n = 1 \ldots \frac{T_s}{T}$, being T_s the given simulation time.

The following code listing shows a Matlab implementation of the algorithm which was described here.

```
clear all
load Evoo.mat; %file containing acquired thrust
               %data over time
%Constants
tsim = 30;          %simulation time
f = 1000;           %sampling rate
tplot = 0:(1/f):tsim; %creates a tsim*f array
                      %using 1/f incrememts
h_0 = 1;            %launch site height
g = 9.8;            %acceleration of gravity
vsom = 340;         %sonic speed (m/s)
Is = 101;           %specific impulse(s)
tq = 4.0;           %burn time (s)
mi = 15;            %initial rocket mass (kg)
A = (pi/4)*(0.1^2)  %rocket transversal area
                    %(m²)
v(1) = 0;
h(1) = 0;
Cd0 = 0.23;
rho_0 = 0.002378 * 515.4; %initial air density
                          %(kg/m³)
%Initializing discrete thrust E[n]
E(1:(tsim*f))=0;
E(1:tq*f) = Evou(401:4400)';
%Initializing discrete mass m[n]
I  = (1/f)*cumsum(E,2);
It = (1/f)*sum(E);
mp = It/(Is*g);     %initial propellant mass
m = mi - mp*(I/It);
%Initializing discrete weight Peso[n]
Peso = m * g;
%To = %air temperature (518.4 R = 15 C)
%b = %temperature-altitude gradient
%   (0.003566R/ft)
%R = %gas constant for the air (53.33089 ft/R)
%rho_0 = 0.002378; %initial air density
%      (slug/ft^3)
%rho(i) =  rho_0*(1-(b/To)*(h_0+h(i)))^((1-
%          b*R)/(b*R));
for i = 1:tsim*f
   rho(i) = rho_0 * (1 - (0.00000688/0.3048) *
        (h_0+h(i))).^ 4.256;
   if v(i) < 238
     Cd(i) = Cd0;      %v < 238
   elseif v(i) < 442
                    %238 <= v < 442
     Cd(i) = 0.32308*log(v(i)/vsom)+0.3452;
   else
     break           %v >= 442
   end
           %drag force
   Fat(i) = 1/2 * Cd(i) * rho(i) * A * (v(i)^2);
          %resultant force
```

```
   Fr(i)  = E(i) - Peso(i) - Fat(i);
   acc(i) = Fr(i) / m(i);          %acceleration
   v(i+1) = v(i) + 1/f * acc(i);  %velocity
   h(i+1) = h(i) + 1/f * v(i);    %height
end
```
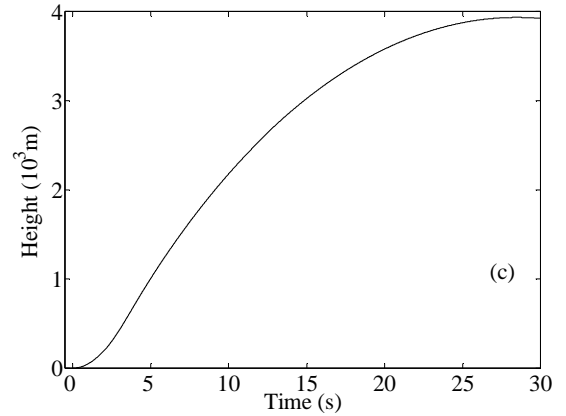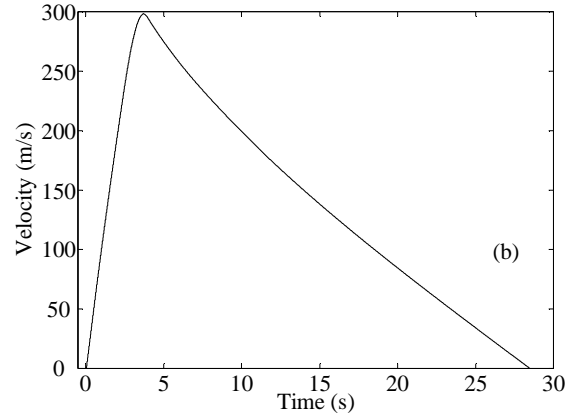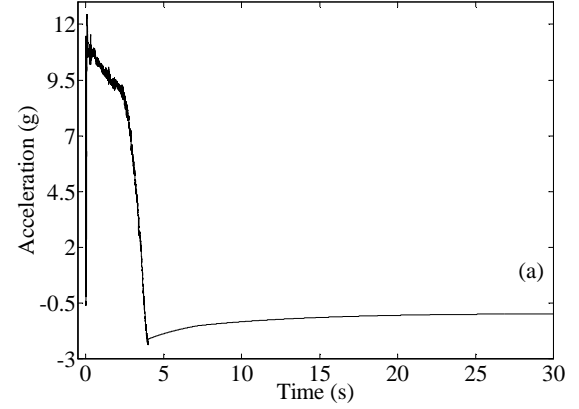

Figure VIII. Acceleration, velocity and height curves as functions of time from an experimental rocket. These curves were generated by simulation.

Figure VIII shows the curves for acceleration, velocity and height as functions of time for a rocket with an initial mass of 15 kg. These data were calculated by the previously described algorithm. By observing curve (a), it can be seen that the maximum acceleration which can be achieved is ~12.4 g, and occurs approximately 0.1 s after ignition. At t ~ 4 s the engine shuts down and the rocket suffers a maximum deceleration of ~ 2.4 g caused by aerodynamic drag and the rocket's weight. By examining curve (b), it can be seen that, moments earlier, at t ~

3.7 s, the rocket reaches its maximum velocity, which is ~298 m/s. After the burn, velocity decreases due to the action of aerodynamic drag and the rocket's weight. The rocket reaches an estimated maximum height of ~ 3933 m at t ~ 28.5 s, as seen in curve (c).

Due to the approximations used in the one-dimensional model, these figures represent an upper bound to the rocket's actual performance figures.

CONCLUSIONS

The experiments presented in this article indicate that a careful procedure to manufacture the propellant grain is responsible for the stability and reproducibility of the generated thrust curves during engine's run. The way propellant is ignited has a significant influence on generated thrust curves. By employing a single igniter or a pair of igniters, the engine's thrust curve can be altered, allowing for its utilization in two distinct operating modes.

The use of a heat shield in the combustion chamber keeps the chamber structure temperatures from reaching critical values when the engine is running and, consequently, pressurized. This allows for a safer operation of the engine and it guaranties its structural integrity. Also this makes possible its reutilization.

The thermal shield also contributes for the engine's improved efficiency in comparison to the performance data of a similar motor described elsewhere[1]. The M44 can generate a total impulse of ~ 4440 Ns. This value is around 55 % greater than the total impulse obtained by that motor's static test[1].

The one-dimensional simulation model of the sounding rocket's flight shows that the engine's performance figures suffice to carry out the mission for which it was designed.

ACKNOLEDGEMENTS

REFERENCES

[1]   STANCATO, F. et al. "A 3000 N.s Solid Rocket Motor Development for Space Education". 51st International Astronautical Congress, Rio de Janeiro, Brazil, October 2-6, 2000. Paper # IAF-00-P.1.06

[2]   STANCATO, F. and MIRAGLIA J. "Internal Ballistic Principles: A Methodology and an Experimental Didactic Experimentation". International Mobility Technology Conference and Exhibit. São Paulo, Brazil, Oct 27-29, 1997. http://www.projetojk.hpg.ig.com.br/SAE2807%20A4.DOC

[3]   HILL, P. and PETERSON, C. "Mechanics and Thermodynamics of Propulsion". 2nd Edition, Addison Wesley Publishing Company, Inc. Reading, 1992

[4]   SUTTON, G. P. "Rocket Propulsion Elements – An Introduction to the Engineering of Rockets". 3rd Edition, John Wiley and Sons, Inc. New York, 1965

[5]   CORNELISSE, J. W., SCHÖYER, H. F. R. and WAKKER, K. F. "Rocket Propulsion and Spaceflight Dynamics". Pitman Publishing Limited, London, 1979

[6]   HUZEL, D. K. and HUANG, D. H. "Modern Engineering for Design of Liquid-Propellant Rocket Engines". Progress in Aeronautics and Astronautics, Vol 147. American Institute of Aeronautics and Astronautics, Inc. Washington, 1992

[7]   POPOV, E. P. "Introdução à Mecânica dos Sólidos". Editora Edgard Blücher Ltda, São Paulo, 1996

[8]   BEJAN, A. "Transferência de Calor". Editora Edgard Blücher Ltda, São Paulo, 1996

[9]   YET-MING C., BIRNIE III, D. and KINGERY W. D. "Physical Ceramics – Principles for Ceramic Science and Engineering". John Wiley and Sons, Inc. New York, 1997

[10]   PÀLLAS-ARENY R. and WEBSTER J. G. "Sensors and Signal Conditioning". 2nd Edition, John Wiley and Sons, Inc. New York, 2001

[11]   VON MISES R. "Theory of Flight". Dover Publications, Inc. New York, 1959

[12]   MARION, J. B. and THORNTON, S. T. "Classical Dynamics of Particles and Systems". 4th Edition, Saunders College Publishing, Fort Worth, 1995